



Cite this: *J. Mater. Chem. B*, 2021, 9, 6068

Two birds with one stone: a NIR fluorescent probe for mitochondrial protein imaging and its application in photodynamic therapy†

Ya-Lin Qi,[‡] Long Guo,[‡] Li-Li Chen, Dan-Dan Yuan, Hai-Rong Wang, Yu-Yao Cao, Yu-Shun Yang* and Hai-Liang Zhu *

Mitochondrial proteins, most of which are encoded in the nucleus and the rest of which are regulated by the mitochondrial genome, play pivotal roles in essential cellular functions. However, fluorescent probes that can be used for monitoring mitochondrial proteins have not yet been widely developed, thereby severely limiting the exploration of the functions of proteins in mitochondria. Towards this end, here we propose a near-infrared (NIR) fluorescence probe **MPP** to effectively illuminate the dynamic changes in mitochondrial proteins in live cells under oxidative stress, with excellent temporal and spatial resolution. Of particular importance, **MPP** extends the study of the pharmacology involved in apoptosis induced by anti-cancer drugs (hydroxycamptothecin (HCPT), epirubicin (Epi) and cyclophosphamide (CPA)) for the first time. Furthermore, employing a protein-activatable strategy, this probe could serve as an excellent phototherapeutic agent in photodynamic therapy (PDT). Finally, *in vivo* experiments suggest that this versatile probe can be used to image tumors in HeLa tumor-bearing mice for 24 h, which demonstrates that our probe could play a dual role as a robust phototherapeutic and imaging agent.

Received 19th April 2021,
Accepted 6th July 2021

DOI: 10.1039/d1tb00881a

rsc.li/materials-b

Introduction

It is well known that mitochondria play vital roles in generating adenosine triphosphate (ATP) to support the entire lifecycle of biological cells and are crucial for cellular life, death, aging and differentiation.¹ Furthermore, they also generate reactive oxidative species (ROS) to actively trigger intracellular signaling pathways.² In the meantime, mitochondrial dysfunction and damage are tightly linked to more than 50 types of serious diseases, including neonatal fatalities, cancer and type II diabetes.³ Thus, it is of great significance to unfold the complex roles mitochondria play in living cells.

On the other hand, mitochondria are organelles with a double-layer membrane structure.⁴ Mitochondrial biogenesis and function are closely linked to membrane proteins with strong hydrophobicity integrated on the inner and outer membranes.⁵ Mitochondria may contain up to 1500 distinct proteins, 13 kinds of which are encoded by the mitochondrial genome, the rest of which must be imported after being synthesized as precursors on cytosolic ribosomes.^{1,6} These proteins are crucial in oxidative phosphorylation, fatty acid

oxidation, the urea cycle, the antioxidant response system, *etc.*⁷ In particular, mutated mitochondrial proteins could lead to damage to the mitochondria.⁸ Furthermore, there is increasing evidence to demonstrate that mitochondrial proteins are closely associated with maternally inherited disorders, aging and neurodegenerative diseases.⁹ On the other hand, it is noteworthy that at least 70% to 80% of drugs exert their efficacy by acting on these membrane/hydrophobic proteins.^{10,11} Therefore, understanding the dynamic behavior of mitochondrial proteins and monitoring their related physiological procedures inside living cells is essential in cell biology, physiology and pharmacology. Up to now, several approaches have been developed for detecting mitochondrial proteins, involving immunoblot assay, mass spectrometry, NMR spectroscopy and immunofluorescence.^{1,11,12} Nonetheless, these typical methods are inconvenient, costly, and incapable of providing real-time information regarding mitochondrial proteins in live cells. Thus, an efficient approach for precisely and vividly detecting mitochondrial protein dynamics is urgently needed.

With operational simplicity and high spatiotemporality, fluorescence imaging has attracted great interest in imaging small biomolecules *in vitro* and *in vivo*.¹³ Recently, Zhang *et al.* reported a versatile fluorescent probe for visualizing mitochondrial nucleoprotein dynamics *via* super-resolution imaging.¹⁴ Nevertheless, the functions of mitochondrial proteins in their work was not further explored. On the other hand, with great biocompatibility, optimal biosafety, desirable therapeutic efficiency and so

State Key Laboratory of Pharmaceutical Biotechnology, School of Life Sciences, Nanjing University, Nanjing, 210023, P. R. China. E-mail: ys_yang@nju.edu.cn, zhuhl@nju.edu.cn

† Electronic supplementary information (ESI) available. See DOI: 10.1039/d1tb00881a

‡ These authors contributed equally to this work.

on, organic small molecules have been recognized as promising agents in photodynamic therapy (PDT).^{15,16} However, only a very few protein-activatable PDT theranostic molecules have been proposed.^{17,18}

Herein, we propose a novel NIR fluorescent probe (named **MPP**) to visualize the dynamic changes in mitochondrial proteins and then participate in PDT. This versatile fluorescent probe was successfully applied for deciphering the crosstalk between H₂O₂ and mitochondrial proteins in live cells. Moreover, facilitated by **MPP**, the pharmacological mechanisms between the three anti-cancer drugs (HCPT, Epi and CPA) and the corresponding proteins have been directly elucidated for the first time. Significantly, this mitochondrial protein responsive theranostic probe shows good potential in PDT. Finally, **MPP** possesses remarkable tumor retention properties *in vivo*. Accordingly, our work presents a novel multifunctional fluorescent probe which not only enabled highly accurate monitoring of mitochondrial proteins, but also led to image-guided photodynamic cancer cell ablation.

Experimental

Materials and equipment

All chemicals were available commercially and the solvents used in the spectral measurement are of chromatographic grade. The ¹H and ¹³C NMR spectra were determined using Bruker DRX-600 and 400 instruments. Fluorescence measurements and UV-vis spectra were performed on a Hitachi Fluorescence Spectrophotometer F-7000 and Shimadzu UV-2550 spectrometer, respectively. The mass spectra were obtained from the Mass Spectrometry Facility at Nanjing University. *In vitro* and *in vivo* imaging were obtained by the live imager of small animals (IVIS Lumina XR, Nanjing University). Mito-tracker (MitoTracker[®] Deep Red FM (MTDR)), Lyso-tracker (LysoBlue), ER-tracker (ER-Tracker Blue-White DPX) and Nucleus-tracker (Hoechst 33342) were available commercially. The imaging experiments were carried out with a confocal fluorescence microscope (Zeiss LSM 980 with Airyscan 2, Zeiss LSM 880 with Airyscan and Olympus FV1000, Nanjing University).

Preparation of the test solution

A stock solution of the probe **MPP** (1.0×10^{-3} M) was prepared in acetonitrile. With hydrophobic pockets, human serum

albumin (HSA) could serve as a model for the mitochondrial proteins.¹⁴ The test solutions of **MPP** (10 μM) containing different concentrations of HSA in phosphate-buffered saline (PBS) buffer (10 mM, pH 7.4, 1% MeCN) were kept at 37 °C for 2 min.

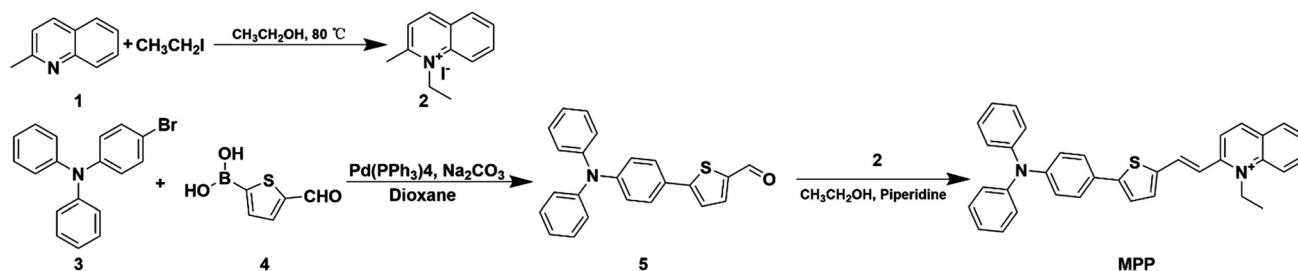
Results and discussion

Molecular design and synthesis

In the probe **MPP**, a triphenylamine (TPA) moiety was selected as an electron-donating (D) unit and this hydrophobic part rendered a fluorescent probe with an extended π conjugation structure.^{19,20} Additionally, the TPA group tended to rotate in the excitation state which endowed **MPP** with prominent twisted intramolecular charge transfer (TICT) properties²¹ and provided a large potential hydrophobic binding site for the hydrophobic protein.²² In particular, a cationic quinolinium group, allowing **MPP** to accumulate in mitochondria, was selected as an electron-accepting (A) unit. In addition, a lipophilic π-conjugated thiophene group²³ and a carbon-carbon double bond worked as a π-bridge, which increased the conjugation length of the platform. With its positive charge, 1-ethylquinolin-1-ium could significantly increase the localization in mitochondria.²⁴ Therefore, we hypothesized that **MPP**, as a multifunctional probe, could be applied for imaging the mitochondrial proteins based on TICT effects and act as a robust PS *in situ*. The synthetic route for **MPP** is depicted in Scheme 1. The chemical structures of **MPP** and the intermediates were fully confirmed by ¹H NMR, ¹³C NMR, and HRMS (Fig. S1–S7, ESI[†]).

Optical properties of MPP and mechanism

As expected, **MPP** (10×10^{-6} M) was initially non-fluorescent when excited at 526 nm owing to the TICT effect, which remarkably quenched its fluorescent emission (Fig. 1A). However, after the addition of HSA (8 mg mL^{-1}) to the above solution, an obviously red emission peak at 659 nm was observed. Meanwhile, there was an absorption band shift from 495 to 515 nm, with a very large Stokes shift ($\Delta\lambda = 144 \text{ nm}$), which ensured minimum interference induced by the excitation light (Fig. 1B). In addition, the fluorescence quantum yield (Φ) of **MPP** was determined to be 0.0034; after incubation with HSA (8 mg mL^{-1}) the value rose to 0.024. The fluorescent response over various pH buffers showed that **MPP** was clearly



Scheme 1 The synthesis route of **MPP**.

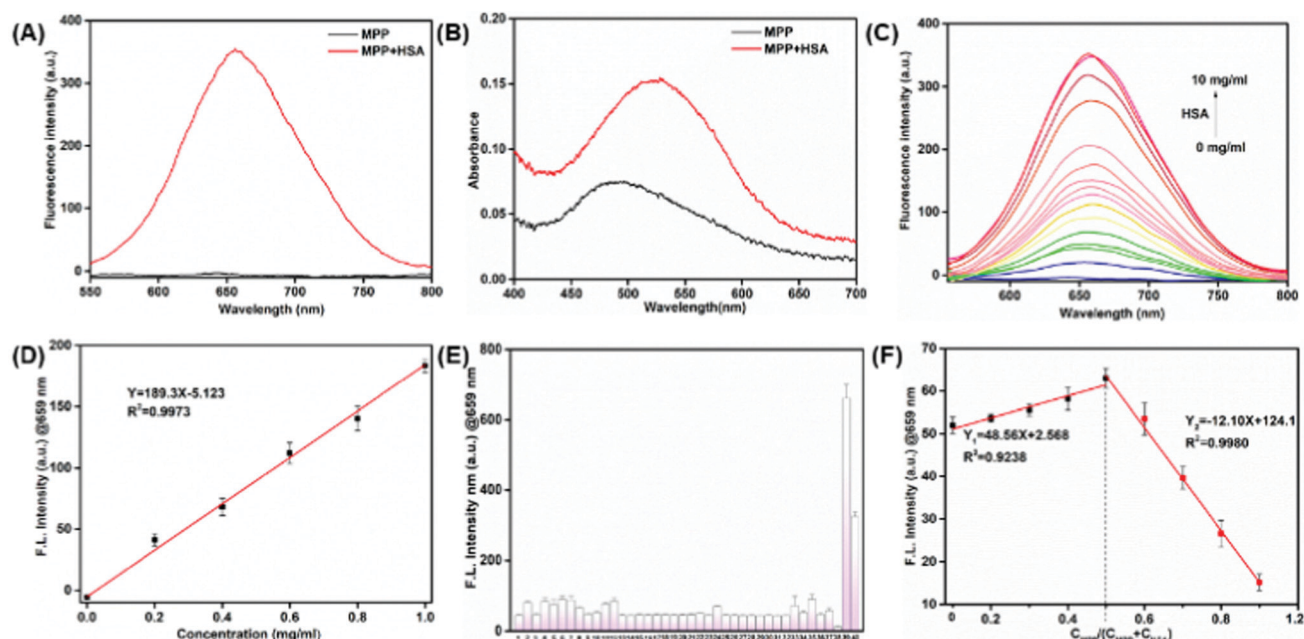


Fig. 1 Response of **MPP** toward HSA. (A) The fluorescence spectra of **MPP** (10×10^{-6} M) incubated with or without HSA (8 mg mL^{-1}). (B) The absorption spectra of **MPP** (10×10^{-6} M) incubated with or without HSA (8 mg mL^{-1}). (C) Fluorescence emission spectra of **MPP** (10×10^{-6} M) incubated with increasing concentrations of HSA ($0\text{--}8 \text{ mg mL}^{-1}$) for 2 min. (D) The linear relationship between the fluorescence intensity and the concentration of HSA ($0\text{--}1.0 \text{ mg mL}^{-1}$). (E) Fluorescence intensity of **MPP** (10×10^{-6} M) at 659 nm incubated with various biological molecules ($2\text{--}26 (10 \times 10^{-4} \text{ M})$, $27\text{--}43 (8 \text{ mg mL}^{-1})$): (1) = blank, (2) = Al^{3+} , (3) = Ca^{2+} , (4) = Cr^{3+} , (5) = Cu^{2+} , (6) = Cu^+ , (7) = Fe^{2+} , (8) = Fe^{3+} , (9) = K^+ , (10) = Mg^{2+} , (11) = Mn^{2+} , (12) = Zn^{2+} , (13) = CH_3COO^- , (14) = Cl^- , (15) = CO_3^{2-} , (16) = F^- , (17) = HCO_3^- , (18) = HSO_3^- , (19) = HSO_4^- , (20) = NO_3^- , (21) = $\text{S}_2\text{O}_3^{2-}$, (22) = SCN^- , (23) = SO_4^{2-} , (24) = ClO^- , (25) = H_2O_2 , (26) = ONOO^- , (27) = Tyr, (28) = His, (29) = Glu, (30) = Pro, (31) = Asp, (32) = Arg, (33) = Ser, (34) = Cys, (35) = GSH, (36) = pepsin, (37) = trypsin, (38) = lysozyme, (39) = hemoglobin, (40) = RNA, (41) = DNA, (42) = BSA, (43) = HSA. (F) Tests for the binding stoichiometry between **MPP** and HSA based on fluorescence intensity at 659 nm. **MPP** and HSA were mixed at different molar ratios while keeping the total concentration constant ($10 \mu\text{M}$). The error bars are \pm standard deviation (SD) from the average of three independent tests.

constant under physiological conditions (Fig. S8, ESI[†]). As shown in Fig. S9 (ESI[†]), a marked enhancement in fluorescence recorded at 659 nm could be clearly obtained after 60 s of incubation, and the enhancement reached a plateau within 200 s. Furthermore, the fluorescence emission intensity with increasing concentrations of HSA ($0\text{--}10 \text{ mg mL}^{-1}$) was also examined (Fig. 1C and Fig. S10, ESI[†]). Notably, there was a good linear relationship ($R^2 = 0.9973$) with HSA concentrations ($0\text{--}1.0 \text{ mg mL}^{-1}$) (Fig. 1D). The limit of detection (LOD) of **MPP** was as low as $34.95 \mu\text{g mL}^{-1}$ (*ca.* 514.3 nM) based on the $3\sigma/\text{slope}$ rule.²⁵ These results suggested that **MPP** shows a fast response to HSA and is highly sensitive toward low concentrations of HSA.

In a selectivity test, the strongest response for albumin proteins and almost no fluorescence changes for other species, including inorganic salts, ROS, and amino acids, were observed, which demonstrated the high specificity of **MPP** toward albumin proteins (Fig. 1E). In particular, there is little interference from proteins without exposed hydrophobic pockets. The selectivity of **MPP** toward albumin proteins affected by inorganic salts, ROS, amino acids and so on was validated in the presence of these interference materials, and the results implied that **MPP** had strong anti-interference ability (Fig. S11, ESI[†]). In addition, the hydrophobicity of **MPP** ($\log P = 2.129$) allowed the probe to bind to hydrophobic pockets in proteins.

All the above results implied that **MPP** had great potential for imaging mitochondrial proteins in living cells, with a rapid response, excellent specificity, high sensitivity and NIR reporting signals.

In order to explore the switch-on mechanism of **MPP** towards HSA, a binding competition experiment was carried out with phenylbutazone and ibuprofen, two classic molecules widely utilized to investigate the interaction with HSA.^{26,27} The fluorescence emission of **MPP** decreased when treated with the Site I binding drug phenylbutazone, whereas no obvious signal change at 659 nm was obtained when incubated with the Site II binding drug ibuprofen (Fig. S12, ESI[†]). These results confirmed that **MPP** was included in Site I of HSA. As shown in the Job's plot analysis, **MPP** could form a complex with HSA in a 1 : 1 (molar ratio) binding stoichiometrically (Fig. 1F). Owing to the fact that increasing solvent viscosity can greatly impede the TICT effect,²⁸ the sensing mechanism of probe **MPP** toward HSA was examined in methanol-glycerol mixed solvents of variable viscosities to verify the existence of the TICT process (Fig. S13, ESI[†]). With increasing viscosity of the medium, the red fluorescence of **MPP** greatly rose, which implied a strong TICT effect. Thus, due to the tight binding of **MPP** into the hydrophobic pocket of HSA, the intramolecular rotation was inhibited and the TICT effect was disrupted within **MPP** upon chelation, which finally led to the obvious turn-on red signal.

In vitro cell imaging

Owing to the fact that dithiothreitol (DTT) can degrade protein structures in live cells, negative experiments were first performed employing DTT.¹⁴ The fluorescence of cells sequentially treated with DTT and **MPP** was obviously reduced compared with the control group (Fig. 2). Undoubtedly, the red fluorescence came from the proteins in mitochondria.

Next, we further investigated the dynamic changes in mitochondrial proteins under oxidative stress. When HeLa cells were treated with H₂O₂ (25 μM) for 60 min and then incubated with **MPP** (4 μM) for 60 min, the red fluorescence obviously decreased compared with the control group (Fig. 3). Previous studies demonstrated that rotenone (Rot) which served as an inhibitor of the oxidative phosphorylation chains in mitochondrial respiration could cause the excess production of H₂O₂.^{29,30} With the stimulation of Rot (20 μM), the red signals of **MPP** remarkably decreased, as expected. In contrast, when the cells were pretreated with Rot for 60 min, then with an ROS scavenger *N*-acetyl cysteine (NAC, 5 × 10⁻⁴ M) for 60 min, and **MPP** for 60 min, a relatively low change in fluorescence signal was obtained compared with a control group which was incubated with **MPP** alone. The results demonstrated that **MPP** was capable of monitoring the dynamic changes in mitochondrial proteins in living cells and proved that the biosynthesis of mitochondrial proteins was tightly correlated with oxidative stress.

It is well known that HCPT, Epi and CPA have been commonly used as antitumor drugs for a variety of cancers,^{31–35} but the relationship between them and mitochondrial proteins at the molecular and protein level have not yet been clarified. Thus, herein we made an effort to explore the molecular mechanism involved in apoptosis induced by those anti-tumor drugs for the

first time *via* the probe **MPP**. Obviously, when HeLa cells were pretreated with Epi and HCPT for 60 min and then incubated with **MPP** (4 μM) for 60 min, remarkable fluorescence enhancement was observed compared with the control group (Fig. 4). Therefore, these results directly suggested that the two agents stimulated the production of mitochondrial proteins during the process of apoptosis. However, CPA led to no significant signal change, which implied that its pharmacological mechanism might be different from the two above-mentioned drugs. As a whole, this study provided abundant and important information about the dynamic changes in the relative expression of mitochondrial proteins before and after apoptosis induced by various antitumor agents. More importantly, it lays a solid foundation for further elucidating the complex roles acted by anti-cancer agents during apoptosis in proteomics research, and paves a new way for understanding the pharmacology of anti-cancer drugs in the future.

In order to evaluate whether **MPP** could still stain mitochondria with decreased mitochondrial membrane potential (MMP), a mitochondrial uncoupling experiment was performed. Carbonyl cyanide *m*-chlorophenylhydrazone (CCCP) is widely utilized to induce rapid acidification of mitochondria to uncouple MMP.³⁶ Live HeLa cells were sequentially incubated with CCCP and **MPP** or in the reverse treatment sequence (**MPP** then CCCP), and, interestingly, no obvious fluorescence change from the control group was obtained (Fig. S14, ESI[†]). Therefore, this phenomenon clearly confirmed the mitochondria-targeting ability of **MPP** and might be illuminated *via* the good lipid solubility of **MPP** as mentioned above and its strong interaction with mitochondrial proteins. Furthermore, we concluded that **MPP** was able to monitor the state of mitochondria under various **MMP** concentrations.

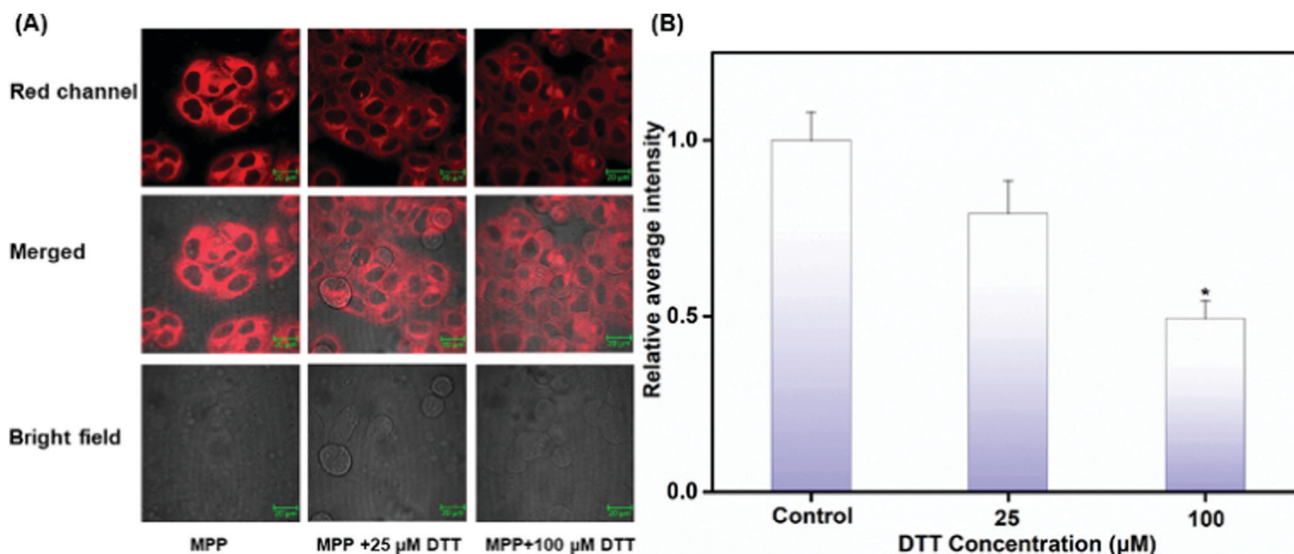


Fig. 2 (A) Negative control adding dithiothreitol DTT (50 μM or 100 μM) to HeLa cells. HeLa cells were first treated with DTT (25 μM and 100 μM) for 60 min, then incubated with **MPP** (4 μM) for 60 min. (B) Quantification of imaging data. $\lambda_{\text{ex}} = 543 \text{ nm}$, $\lambda_{\text{em}} = 600\text{--}750 \text{ nm}$. The error bars are \pm standard deviation (SD) from the average of five independent tests. Statistical analyses were employed with a two-tailed Student's *t*-test with unequal variance, **p*-value < 0.05. Scale bar: 20 μm.

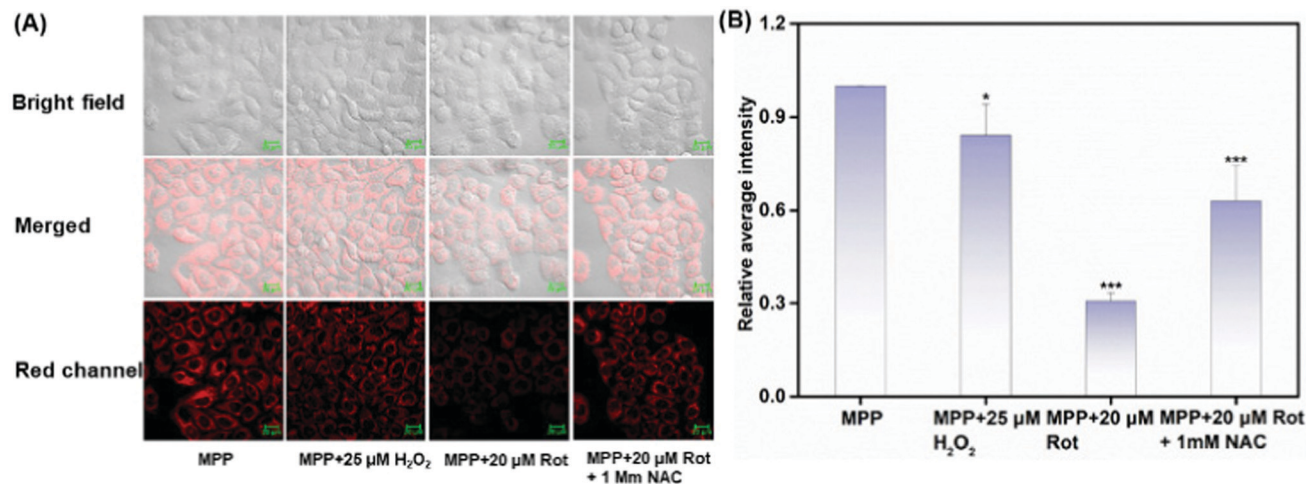


Fig. 3 (A) Fluorescent signals upon the addition of endogenous and exogenous H₂O₂. (B) Quantification of imaging data. $\lambda_{\text{ex}} = 543 \text{ nm}$, $\lambda_{\text{em}} = 600\text{--}750 \text{ nm}$. The error bars are \pm standard deviation (SD) from the average of five independent tests. Statistical analyses were employed with a two-tailed Student's *t*-test with unequal variance, **p*-value < 0.05, ****p*-value < 0.001. Scale bar: 20 μm .

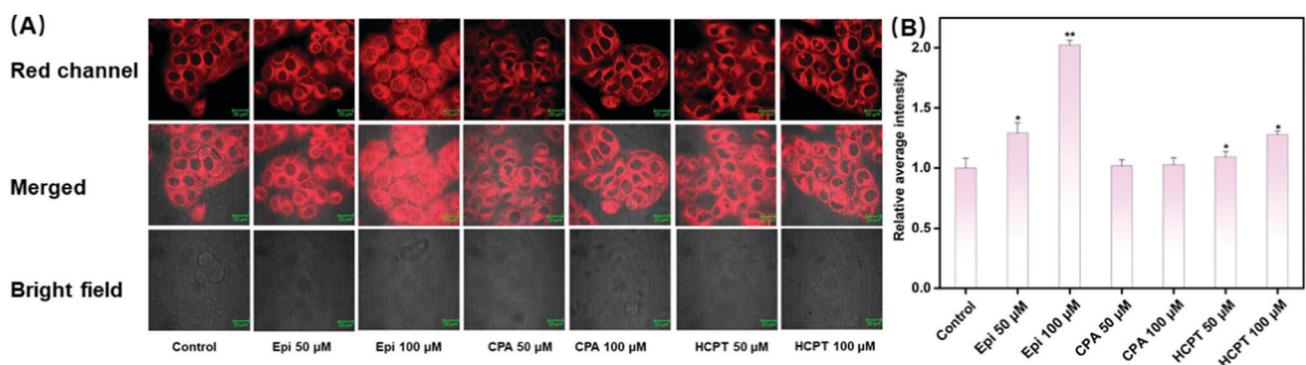


Fig. 4 (A) Characterization of **MPP** for imaging the effect of anti-tumor drugs on mitochondrial proteins in living HeLa cells. HeLa cells were first treated with Epi (50 μM or 100 μM), CPA (50 μM or 100 μM) or HCPT (50 μM or 100 μM) for 60 min separately, then incubated with **MPP** (4 μM) for 60 min. (B) Quantification of imaging data. $\lambda_{\text{ex}} = 543 \text{ nm}$, $\lambda_{\text{em}} = 600\text{--}750 \text{ nm}$. The error bars are \pm standard deviation (SD) from the average of five independent tests. Statistical analyses were employed with a two-tailed Student's *t*-test with unequal variance, **p*-value < 0.05, ***p*-value < 0.01. Scale bar: 20 μm .

To characterize the intracellular distribution of **MPP**, HeLa cells were co-incubated with **MPP** and various commercial organelle-targeting probes. As expected, the fluorescence images from cells treated with **MPP** mainly overlapped with those of the Mito-Tracker over Lyso- or ER- or Nucleus-Tracker (Pearson's correlation coefficients were 0.78, 0.52, 0.38 and 0.26, respectively), suggesting the major distribution of **MPP** in mitochondria (Fig. S15, ESI[†]). In particular, the Pearson's correlation coefficient of **MPP** in mitochondria not being very high might be caused by **MPP** showing granular fluorescent spots in mitochondria.

As shown in Fig. S16 (ESI[†]), the photostability of **MPP** was investigated in living cells. Indeed, **MPP** performed with even better photostability than the commercial mitochondria dye MTDR within 150 s, which implied that the former showed higher resistance to photobleaching.

Evaluation of PDT efficacy

Typically, the strong D–A effect can greatly promote NIR emission, leading to separation of the highest occupied molecular

orbital (HOMO) and lowest unoccupied molecular orbital (LUMO) distribution and reduction of singlet–triplet energy gaps (ΔE_{ST}), which effectively promotes ROS generation.³⁷ Furthermore, spin–orbit coupling (SOC) and ΔE_{ST} are key factors in promoting intersystem crossing (ISC) to increase ROS production.³⁸ Hence, the SOC effect and ΔE_{ST} were calculated by time-dependent density functional theory (TD-DFT) at the B3LYP/6-311G(d) level (Table S1, ESI[†]). As illustrated in Fig. S17 (ESI[†]), ΔE_{S1T2} was determined to be 0.298 eV with an SOC of 0.21 cm^{-1} , which indicated that the ISC process was possible before T₂ to T₁ internal conversion (IC) took place. Thus, it was safe to conclude that **MPP** was capable of generating ROS with high efficiency. Then, we evaluated the ROS generation capability of **MPP** with 2',7'-dichlorodihydrofluorescein diacetate (H2DCF-DA) upon light illumination (17 W m^{-2}) for 0 min, 5 min and 10 min in PBS for its ability to generate fluorescence at 525 nm after being oxidized by ROS.³⁹ As shown in Fig. 5A, solutions of H2DCF-DA (10 μM) containing HSA (8 mg mL^{-1}) and **MPP** (10 μM) respectively exhibited no

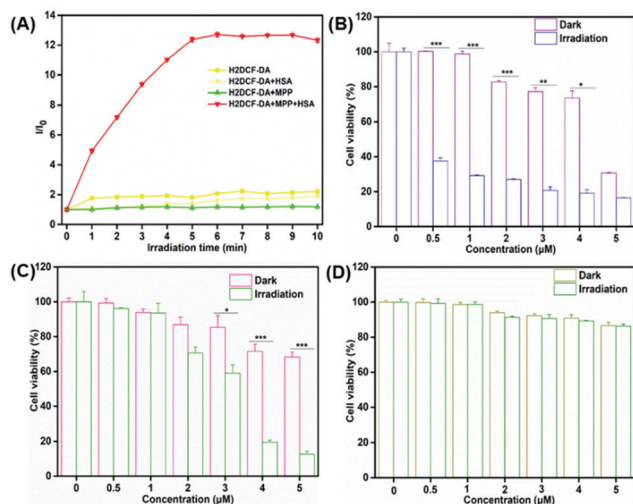


Fig. 5 ROS generation upon light illumination and the PDT assessment of MPP. (A) Relative change in fluorescence intensity (I/I_0) at 525 nm of H2DCF-DA, mixtures of H2DCF-DA and MPP, mixtures of H2DCF-DA and HSA, and mixtures of H2DCF-DA, HSA and MPP in PBS upon light illumination for various times (0–10 min). Concentrations: 4 μM (MPP) and 10 μM (H2DCF-DA). (B) Survival rates of HeLa cells stained with various concentrations of MPP with or without green light illumination for 10 min. (C) Survival rates of MCF-7 cells incubated with various concentrations of MPP with or without green light illumination for 10 min. (D) Survival rates of 293T cells incubated with various concentrations of MPP with or without green light illumination for 10 min. Light power: 17 W m^{-2} . The error bars are \pm standard deviation (SD) from the average of five independent tests. Statistical analyses were employed with a two-tailed Student's t -test with unequal variance, * p -value < 0.05, ** p -value < 0.01, *** p -value < 0.001.

apparent fluorescence enhancement, while co-incubation of HSA and MPP led to a 12-fold enhancement within 6 min, which indicated that the ROS generation ability of MPP could be activated by HSA, as we expected, and the ROS generation was efficient. In addition, the singlet oxygen ($^1\text{O}_2$) generation ability of MPP was analysed with 1,3-diphenylisobenzofuran (DPBF) as the $^1\text{O}_2$ trapping agent.⁴⁰ In the presence of MPP and HSA under irradiation, the absorbance of DPBF at 425 nm decreased remarkably, while no significant decline in absorbance was found in the presence of HSA (Fig. S18, ESI[†]). The singlet oxygen quantum yield (Φ) of MPP in MeCN/PBS ($v/v = 1/199$) was calculated to be 0.52 with Rose Bengal (RB) as the standard ($\Phi = 0.75$ in water)⁴¹ (Fig. S19, ESI[†]).

Inspired by the remarkable performance of MPP for ROS production, we tested three different cell lines, HeLa, MCF-7 and 293T, by standard MTT assay to further test the phototherapy efficacy of MPP. As reflected in Fig. 5B and C, MPP showed substantial phototoxicity upon light illumination (17 W m^{-2}) to HeLa cells, while slightly lower phototoxicity was generated to MCF-7 cells. Evidently, negligible biotoxicity and phototoxicity to 293T normal cells was found with or without green light irradiation (Fig. 5D). Notably, under green light illumination, the IC_{50} value (inhibitory concentration of 50% cell death) of the probe toward HeLa cells was 0.163 μM , which was 19-fold lower than that of the probe in the dark (3.142 μM). And the IC_{50} values of MPP under light were determined to be

2.757 and 20.187 μM to MCF-7 and 293T cells, respectively. Meanwhile, the values were 8.449 and 22.438 μM toward the two above-mentioned cell lines in the dark, separately. It was particularly noteworthy that MPP possessed selective toxicity to normal cells (293T) and cancer cells (HeLa and MCF-7 cells). According to these results, we rationally hypothesized that this result was attributable to the fact that levels of mitochondrial proteins in HeLa cells might be higher than those in MCF-7 cells and normal cells. Besides, previous reports showed that carcinoma cells exhibit more negative mitochondrial membrane potential than normal cells.^{42,43} Furthermore, we believed that HeLa cells might have higher negative mitochondrial membrane potential than MCF-7 cells. Collectively, owing to both the high levels of mitochondrial proteins and negative mitochondrial membrane potential in HeLa cells, MPP possessed specific phototoxicity toward this type of cells. Thus, this feature equipped the MPP with desirable biocompatibility and biosafety as a promising theranostic agent for *in vivo* applications. Next, we compared the phototoxicity of MPP and RB to HeLa cells. As shown in Fig. S20 (ESI[†]), no obvious phototoxicity was observed in HeLa cells after incubation with RB. Moreover, the IC_{50} values of RB under light and in the dark were calculated to be 6.601 and 7.081 μM to HeLa cells, respectively. Thus, MPP presented higher PDT efficiency than RB.

Additionally, flow cytometry analysis by Annexin V-FITC and PI was used to determine cell apoptosis. The percentages of HeLa cells treated by MPP (10 μM) in the apoptotic region for 0 min, 5 min and 10 min were 5.2%, 10.3% and 39%, respectively (Fig. 6A). In particular, upon light irradiation (17 W m^{-2}), the apoptotic percentages of HeLa cells incubated with MPP (4 μM) for 10 min were about 8-fold larger than those of the control group (Fig. 6B). Furthermore, intracellular ROS detection was performed by using H2DCF-DA as an indicator. A strong green signal was obtained in the group incubated with H2DCF-DA (10 μM) and MPP (4 μM) under light illumination for 5 min, whereas no noticeable fluorescence signals were obtained in other groups (Fig. S21, ESI[†]). As a whole, these data

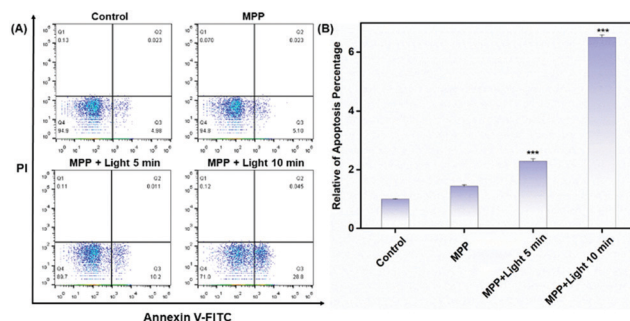


Fig. 6 The PDT study of MPP (4 μM) by flow cytometry analysis. (A) Apoptosis analysis by Annexin V-FITC/PI double staining after light illumination for different times (0 min, 5 min and 10 min). (B) Relative apoptosis percentage in (A). The error bars were \pm standard deviation (SD) from the average of three independent tests. Statistical analyses were employed with a two-tailed Student's t -test with unequal variance, *** p -value < 0.001.

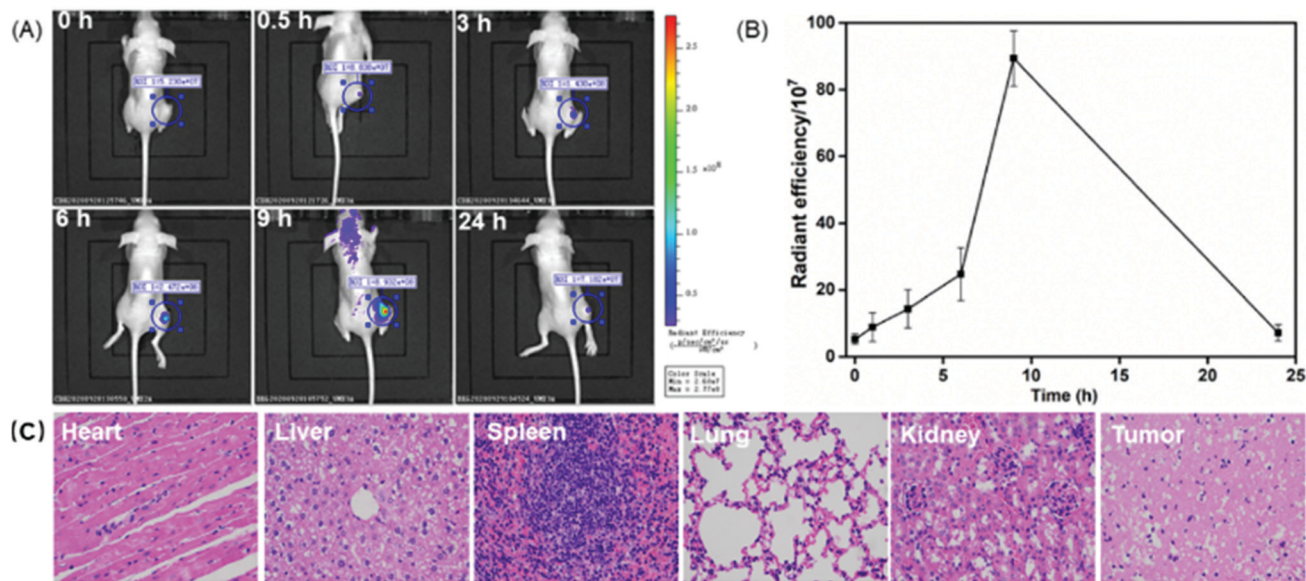


Fig. 7 *In vivo* imaging and cytotoxicity test. (A) Biodistribution of MPP in HeLa tumor-bearing mice after intratumoral injection of MPP (10 μ M, 50 μ L) at various times. (B) The radiant efficiency of HeLa tumor-bearing mice after intratumoral injection of MPP (10 μ M, 50 μ L) at various times in (A). (C) H&E-staining analysis of organ slices from mice in (A). The mice were sacrificed at 24 h post-injection. Excitation filter: 535 nm; emission filter: DsRed, 575–650 nm. The error bars are \pm standard deviation (SD) from the average of three independent tests.

demonstrated that MPP produced a large number of ROS under light illumination and showed great potential as a robust agent for PDT.

In vivo imaging experiment

Aiming to achieve a versatile probe with integrated functionalities of phototheranostics and imaging-guided precision surgery, the ability of tumor imaging by MPP was investigated *in vivo* by an imaging experiment. As depicted in Fig. 7A and B, fluorescence signals reached a peak at 9 h after the injection of MPP (10 μ M), which suggested ideal tumor retention properties. Moreover, MPP could accumulate at the tumour region with good specificity at 24 h postinjection (Fig. S22, ESI[†]). And H&E-stained organ slices proved the negligible toxicity to organisms of MPP (Fig. 7C).

Conclusions

In conclusion, we have reported a versatile NIR fluorescence probe, MPP, to track mitochondrial protein activity in live cells and to participate in PDT. This multifunctional probe was able to monitor the dynamic changes in mitochondrial proteins during oxidative stress. Furthermore, using this probe, for the first time a study of the pharmacology involved in apoptosis induced by anti-cancer drugs (HCPT, Epi and CPA) was conducted. The results disclosed that HCPT and Epi could promote the upregulation of mitochondrial proteins, while no obvious changes were generated by CPA during apoptosis. Meanwhile, MPP showed great potential as a robust PS with excellent ROS generation ability. Finally, we successfully applied MPP for tumor imaging after about 24 h, attesting to its dual function as an eminent phototherapeutic and imaging agent. This work

might pave a new way for the design of novel fluorescent probes to unveil the essential roles of mitochondrial proteins in cell biology and physiology, and provide a promising versatile tool for imaging-guided precision therapy.

Conflicts of interest

There are no conflicts to declare.

Acknowledgements

The authors gratefully acknowledge the financial support from the Major Science and Technology Program for Water Pollution Control and Treatment, China (No. 2017ZX07602-002). The first author Ya-Lin Qi is very grateful for the help from Master Li-Li Chen and Master Hai-Rong Wang.

References

- 1 D. J. Pagliarini, S. E. Calvo, B. Chang, S. A. Sheth, S. B. Vafai, S. E. Ong, G. A. Walford, C. Sugiana, A. Boneh, W. K. Chen, D. E. Hill, M. Vidal, J. G. Evans, D. R. Thorburn, S. A. Carr and V. K. Mootha, *Cell*, 2008, **134**, 112–123.
- 2 J. K. Andersen, *Nat. Med.*, 2004, **10**, S18–S25.
- 3 N. Zhu, G. Xu, R. Wang, T. Zhu, J. Tan, X. Gu and C. Zhao, *Chem. Commun.*, 2020, **56**, 7761–7764.
- 4 D. Tomasek, S. Rawson, J. Lee, J. S. Wzorek, S. C. Harrison, Z. Li and D. Kahne, *Nature*, 2020, **583**, 473–478.
- 5 C. U. Mårtensson, C. Priesnitz, J. Song, L. Ellenrieder, K. N. Doan, F. Boos, A. Floerchinger, N. Zufall, S. Oeljeklaus, B. Warscheid and T. Becker, *Nature*, 2019, **569**, 679–683.

- 6 R. Di Maio, P. J. Barrett, E. K. Hoffman, C. W. Barrett, A. Zharikov, A. Borah, X. Hu, J. McCoy, C. T. Chu, E. A. Burton, T. G. Hastings and J. T. Greenamyre, *Sci. Transl. Med.*, 2016, **8**, 1–15.
- 7 A. S. Hebert, K. E. Dittenhafer-Reed, W. Yu, D. J. Bailey, E. S. Selen, M. D. Boersma, J. J. Carson, M. Tonelli, A. J. Balloon, A. J. Higbee, M. S. Westphall, D. J. Pagliarini, T. A. Prolla, F. Assadi-Porter, S. Roy, J. M. Denu and J. J. Coon, *Mol. Cell*, 2013, **49**, 186–199.
- 8 S. M. Yoo and Y. K. Jung, *Mol. Cells*, 2018, **41**, 18–26.
- 9 L. Ruan, C. Zhou, E. Jin, A. Kucharavy, Y. Zhang, Z. Wen, L. Florens and R. Li, *Nature*, 2017, **543**, 443–446.
- 10 S. Da Cruz, I. Xenarios, J. Langridge, F. Vilbois, P. A. Parone and J. C. Martinou, *J. Biol. Chem.*, 2003, **278**, 41566–41571.
- 11 B. Devreese, F. Vanrobaeys, J. Smet, J. V. Beeumen and R. V. Coster, *Electrophoresis*, 2002, **23**, 2525–2533.
- 12 M. J. Berardi, W. M. Shih, S. C. Harrison and J. J. Chou, *Nature*, 2011, **476**, 109–114.
- 13 J.-B. Li, H.-W. Liu, T. Fu, R. Wang, X.-B. Zhang and W. Tan, *Trends Chem.*, 2019, **1**, 224–234.
- 14 G. Yang, Z. Liu, R. Zhang, X. Tian, J. Chen, G. Han, B. Liu, X. Han, Y. Fu, Z. Hu and Z. Zhang, *Angew. Chem., Int. Ed.*, 2020, **59**, 16154–16160.
- 15 L. Wu, J. Liu, P. Li, B. Tang and T. D. James, *Chem. Soc. Rev.*, 2021, **50**, 702–734.
- 16 M. Li, J. Xia, R. Tian, J. Wang, J. Fan, J. Du, S. Long, X. Song, J. W. Foley and X. Peng, *J. Am. Chem. Soc.*, 2018, **140**, 14851–14859.
- 17 V. N. Nguyen, S. Qi, S. Kim, N. Kwon, G. Kim, Y. Yim, S. Park and J. Yoon, *J. Am. Chem. Soc.*, 2019, **141**, 16243–16248.
- 18 X. Li, C. Y. Kim, S. Lee, D. Lee, H. M. Chung, G. Kim, S. H. Heo, C. Kim, K. S. Hong and J. Yoon, *J. Am. Chem. Soc.*, 2017, **139**, 10880–10886.
- 19 J. Yin, M. Peng, Y. Ma, R. Guo and W. Lin, *Chem. Commun.*, 2018, **54**, 12093–12096.
- 20 Y. Wu, P. Jin, K. Gu, C. Shi, Z. Guo, Z.-Q. Yu and W.-H. Zhu, *Chem. Commun.*, 2019, **55**, 4087–4090.
- 21 R. Zhang, G. Niu, Z. Liu, J. H. C. Chau, H. Su, M. M. S. Lee, Y. Gu, R. T. K. Kwok, J. W. Y. Lam and B. Z. Tang, *Biomaterials*, 2020, **242**, 119924.
- 22 S. Samanta, M. Huang, F. Lin, P. Das, B. Chen, W. Yan, J.-J. Chen, K. Ji, L. Liu, J. Qu and Z. Yang, *Anal. Chem.*, 2020, **92**, 1541–1548.
- 23 S. Ma, G. Chen, J. Xu, Y. Liu, G. Li, T. Chen, Y. Li and T. D. James, *Coord. Chem. Rev.*, 2021, **427**, 213553.
- 24 D. Cheng, J. Peng, Y. Lv, D. Su, D. Liu, M. Chen, L. Yuan and X. Zhang, *J. Am. Chem. Soc.*, 2019, **141**, 6352–6361.
- 25 Y.-L. Qi, L.-L. Chen, L. Guo, C. Shao, Y. Liu, Y.-S. Yang, Z.-X. He and H.-L. Zhu, *Chem. – Asian J.*, 2020, **15**, 3551–3557.
- 26 X. Chai, H. H. Han, A. C. Sedgwick, N. Li, Y. Zang, T. D. James, J. Zhang, X. Le Hu, Y. Yu, Y. Li, Y. Wang, J. Li, X. P. He and H. Tian, *J. Am. Chem. Soc.*, 2020, **142**, 18005–18013.
- 27 L. Yang, J. Zheng, Z. Zou, H. Cai, P. Qi, Z. Qing, Q. Yan, L. Qiu, W. Tan and R. Yang, *Chem. Commun.*, 2020, **56**, 1843–1846.
- 28 Y. Zhang, C. Yan, C. Wang, Z. Guo, X. Liu and W.-H. Zhu, *Angew. Chem., Int. Ed.*, 2020, **59**, 9059–9066.
- 29 M. Tian, J. Sun, B. Dong and W. Lin, *Angew. Chem., Int. Ed.*, 2018, **57**, 16506–16510.
- 30 Y. Lu, B. Peng, X. Qiu, X. Li, Z. Li, D. Zhang, W. Ji, B. Fang, Q. Wu, C. Zhang, L. Li and W. Huang, *Mater. Adv.*, 2020, **1**, 1448–1454.
- 31 A. V. Patterson, D. M. Ferry, S. J. Edmunds, Y. Gu, R. S. Singleton, K. Patel, S. M. Pullen, K. O. Hicks, S. P. Syddall, G. J. Atwell, S. Yang, W. A. Denny and W. R. Wilson, *Clin. Cancer Res.*, 2007, **13**, 3922–3932.
- 32 Y. Mao, E. T. Keller, D. H. Garfield, K. Shen and J. Wang, *Cancer Metastasis Rev.*, 2013, **32**, 303–315.
- 33 Z. Guo, C. Yan and W. Zhu, *Angew. Chem., Int. Ed.*, 2020, **59**, 9812–9825.
- 34 Y. R. Fu, Z. J. Yi, Y. R. Yan and Z. Y. Qiu, *Mitochondrion*, 2006, **6**, 211–217.
- 35 Y. R. Fu, Z. J. Yi, Y. R. Yan and Z. Y. Qiu, *Anticancer Drugs*, 2007, **18**, 1045–1052.
- 36 R. Zhang, G. Niu, X. Li, L. Guo, H. Zhang, R. Yang, Y. Chen, X. Yu and B. Z. Tang, *Chem. Sci.*, 2019, **10**, 1994–2000.
- 37 Y. Dai, F. He, H. Ji, X. Zhao, S. Misal and Z. Qi, *ACS Sens.*, 2020, **5**, 225–233.
- 38 Z. Liu, H. Zou, Z. Zhao, P. Zhang, G. G. Shan, R. T. K. Kwok, J. W. Y. Lam, L. Zheng and B. Z. Tang, *ACS Nano*, 2019, **13**, 11283–11293.
- 39 Z. Zhou, J. Liu, J. Huang, T. W. Rees, Y. Wang, H. Wang, X. Li, H. Chao and P. J. Stang, *Proc. Natl. Acad. Sci. U. S. A.*, 2019, **116**, 20296–20302.
- 40 Q. Zhang, S. Xu, F. Lai, Y. Wang, N. Zhang, M. Nazare and H. Y. Hu, *Org. Lett.*, 2019, **21**, 2121–2125.
- 41 D. Wang, H. Su, R. T. K. Kwok, X. Hu, H. Zou, Q. Luo, M. M. S. Lee, W. Xu, J. W. Y. Lam and B. Z. Tang, *Chem. Sci.*, 2018, **9**, 3685–3693.
- 42 Q. Hu, M. Gao, G. Feng and B. Liu, *Angew. Chem., Int. Ed.*, 2014, **53**, 14225–14229.
- 43 J. Dai, X. Wu, S. Ding, X. Lou, F. Xia, S. Wang and Y. Hong, *J. Med. Chem.*, 2020, **63**, 1996–2012.